Model Predictive Controller and Multilevel Inverter Design for Grid Voltage Unbalance Resilience Model in Brushless Doubly-Fed Induction Generator-Based Wind Turbines

Dr. ANKA RAO MOGILI[1], M.Tech., Ph.D, **Y.SHIVA PRASAD**[2],
[1]Assistant Professor, Department of EEE, JNTUA College of Engineering, Anathapuramu, India.
[2]PG Student, (Power and Industrial Drives), Department of EEE, JNTUA College of Engineering, Anathapuramu, India

ABSTRACT: This paper aims to enhance the resilience of Brushless Doubly-Fed Induction Generator (BDFIG)-based wind turbines against grid voltage unbalance using a Model Predictive Controller (MPC) and a Multilevel Inverter (MLI). Grid voltage unbalance can destabilize wind turbines, increasing system stress and potential grid instability. The MPC algorithm enables real-time monitoring and control adjustments based on predicted system behavior, mitigating these effects. The MLI improves voltage regulation and reduces harmonics by providing higher voltage levels and lower switching frequencies compared to traditional inverters. Through detailed modeling and coordinated control design, this paper seeks to boost the robustness and reliability of BDFIG-based wind turbines, ensuring stable operation under varying grid conditions and enhancing grid stability.

KEYWORDS: Brushless Doubly-Fed Induction Generator (BDFIG), voltage unbalance, decoupling control, wind turbine, sequence decomposition, Model Predictive Controller (MPC), Multilevel Inverter (MLI).

NOMENCLATURE:

v_p, v_c	voltage vectors of power windings (PW)and control windings (CW).
I_p, I_c, I_r	Current vectors of PW, CW, and rotor.
ψ_p, ψ_c, ψ_r	Flux vectors of PW, CW and rotor.
ω_p, ω_c	Electrical angular frequency of PW and CW.
θ_r, ω_r,	Mechanical angle, angular frequency of rotor.
p_p, p_c	Pole pairs of PW and CW.
V_g, I_g	Grid voltage and current vectors of GSC.
V_{dc}	DC link Voltage.
I_{total}	Total output current of wind turbine system.
P_p, Q_p	output active and reactive power of PW.
P_g, Q_g	output active and reactive power of GSC.
P_{total} Q_{total}	Total output active and reactive power of BDFIG-based wind turbine system.
T_e	Electromagnetic torque of BDIFG.
R_p, R_c, R_r	PW, CW, and rotor windings (RW) resistance.
L_p, L_c, L_r	Self-inductance of PW, CW, and RW.
L_{pr} L_{cr}	Mutual inductance between stator and rotor.
R_g L_g	Resistance, inductance of GSC filter.
θp, θg	Vector angle of PW flux and grid voltage.
Superscripts	
+, -	Positive, negative (dq) reference frame.
*	Reference value for controller.
—	Conjugate complex.
Subscripts	
α_p, β_p	PW stationary α-β axis.
α_r, β_r	RW α-β axis.
α_c, β_c	CW α-β axis.
d, q	Synchronous d-q axis.
p, r, c	PW, RW and CW.
+, −	Positive, negative sequence components.

I.INTRODUCTION:

The brushless Double-fed Ignition Generator (BDFIG) is an apparatus that gaining attention as a superior alternative to traditional slip-ring doubly-fed induction generators (DFIGs). BDFIGs are more reliable and require less lack of brush and sliding rings, which requires more maintenance. More features include improved low voltage ride-through and smaller mechanical gears. (LVRT) capabilities, making them ideal for remote or offshore wind energy systems where maintenance is difficult and costly.

Despite previous research on BDFIGs under balanced grid conditions, real-world voltage imbalances from asymmetrical loads or faults pose significant challenges. These imbalances can cause severe current issues, power oscillations, and system instability. To address this, grid codes now mandate wind turbines to handle voltage unbalances without tripping. This study focuses on improving control strategies for grid-connected BDFIG systems under such conditions, proposing a coordinated control strategy between both the grid-side converter and the machine-side conversion (MSC) (GSC). This new strategy aims to enhance system stability and performance, meeting grid requirements under unbalanced conditions.

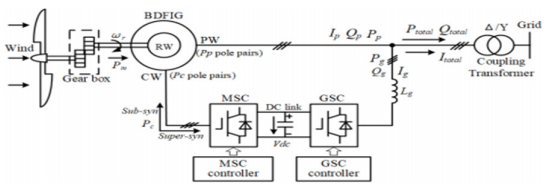

FIGURE 1. Configuration of BDFIG- based wind turbine system.

The wind power system known as BDFIG. control is enhanced to handle grid imbalances better. It eliminates torque oscillations and allows choosing between three objectives: balanced output current, stable output active power, or reactive power. Simplified single current loop

controllers for MSC and GSC improve robustness and decouple control of active and reactive power, enhancing dynamic response. A fast sequence decomposition approach further refines control. The paper covers system configuration, mathematical modeling, coordinated control methods, and case studies for a 2MW turbine.

II. BDFIG-based wind turbine configuration and fundamental operating principles.

The BDFIG turbine system is composed of the following components: a choke inductor, coupling transformer, gearbox, BDFIG, and a back-to-back converter with MSC and GSC.. The BDFIG has rotor windings (RW) in addition to two stator windings, output the windings (PW) along with control windings (CW).

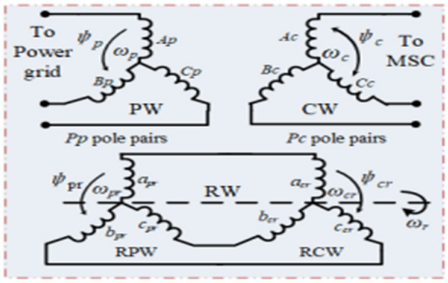

FIGURE2. Three phase windings ofBDFIG

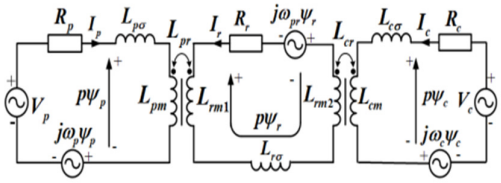

FIGURE 3The equivalent BDFIG circuit in the PW reference frame. and the rotor control windings (RCW), which are connected to PW and CW, respectively, through a magnetic coupling.

Figure 1 shows PW directly With a DC link, CW is stimulated by MSC and GSC, but it is linked to the power grid. Figure 2 illustrates BDFIG's air-gap magnetic fields, with fluxes rotating at specific speeds. The synchronous

condition is met with ωp is equal to ωpr + ppωr, while ωc is equal to ωcr + pcωr. ωpr = −ωcr, which results in ωp because RPW and RCW are in an inverse phase sequence. as shown.

$$\omega_p = -\omega_c + (p_p + p_c)\,\omega_r \quad (1)$$

To keep ωp constant, ωc must change directly with ωr. At ωc = 0, the rotor spins at the synchronous speed of nature ωN.

$$\omega_N = \omega_p/(p_p + p_c) \quad (2)$$

III. BDFIG turbine system modelling with unbalanced grid voltage.

(A). The grid voltage imbalance vectors model for BDFIG (MSC).

The dynamic vector model of a BDFIG in the dq reference frame, rotating at angular speed ωp, is derived from its equivalent circuit diagram shown in Fig. 3.

$$V_p = R_p I_p + p\psi_p + j\omega_p\psi_p \quad (3)$$

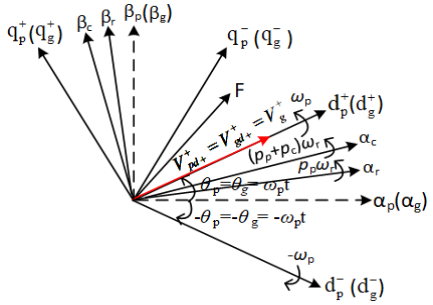

FIGURE 4. Relationships between the (αpβp), (αgβg), (αr βr), (αcβc) and the (dq) + and (dq) − reference frames.

$$V_r = R_r I_r + p\psi_r + j\omega_{pr}\psi_r \quad (5)$$

$$\psi_p = \text{LpIp+LprIr} \quad (6)$$

$$\psi_c = \text{LcIc-LcrrIr} \quad (7)$$

$$\psi c = LrI\,r + LprIp - LcrIc \quad (8)$$

In this context, frequencies and inductances of primary (PW), rotor (RW), and control (CW) windings are related through specific equations. Magnetizing inductances are denoted by Lpm, Lrm1, Lrm2, and Lcm, while leakage inductances are Lpσ, Lrσ, and Lcσ.

the vector F transformations between several reference frames, including voltage, current, and flux, can be derived as

$$F^{+}_{d_pq_p} = F_{\alpha_p\beta_p} e^{-j\omega_p t} \quad F^{-}_{d_pq_p} = F_{\alpha_p\beta_p} e^{j\omega_p t} \quad (9)$$

$$F^{+}_{d_pq_p} = F^{-}_{d_pq_p} e^{-j2\omega_p t} \quad F^{-}_{d_pq_p} = F^{+}_{d_pq_p} e^{j2\omega_p t} \quad (10)$$

$$F^{+}_{d_pq_p} = F_{\alpha_r\beta_r} e^{-j\omega_{pr} t} \quad F^{-}_{d_pq_p} = F_{\alpha_r\beta_r} e^{j\omega_{pr} t} \quad (11)$$

$$F^{+}_{d_pq_p} = F_{\alpha_c\beta_c} e^{-j\omega_c t} \quad F^{-}_{d_pq_p} = F_{\alpha_c\beta_c} e^{j\omega_c t} \quad (12)$$

TABLE 1.Frequencies of PW, RW and CW quantities.

	PW frequency	RW frequency	CW frequency
Positive component	ωp	ωp_r	ω_c
Negative component	-ωp	-2ωp+ ω_{pr}	-2ωp+ ωc

sequence component and can be expressed as [15]

$$F_{\alpha_p\beta_p} = F_{\alpha_p\beta_{p+}} + F_{\alpha_p\beta_{p-}} = f_{m+} e^{j\omega_p t} + f_{m-} e^{-j\omega_p t} \quad (13)$$

$$F^{+}_{dq} = F^{+}_{dq+} + F^{-}_{dq-} e^{-j2\omega_p t}$$
$$F^{-}_{dq} = F^{-}_{dq-} + F^{+}_{dq+} e^{j2\omega_p t} \quad (14)$$

According to (14), in the (dpqp)+ or (dpqp)− reference frame, the vector F includes both steady-state and double-frequency oscillating terms. This implies that negative sequence

components in unbalanced grid voltage cause authority, acceleration, and DC link fluctuations in voltage at substantial double frequencies.

$$V_{pdq}^{+} = R_p I_{pdq}^{+} + p\psi_{pdq}^{+} + j\omega_p \psi_{pdq}^{+} \quad (15a)$$
$$V_{cdq}^{+} = R_c I_{cdq}^{+} + p\psi_{cdq}^{+} + j\omega_c \psi_{cdq}^{+} \quad (15b)$$
$$0 = R_r I_{rdq}^{+} + p\psi_{rdq}^{+} + j\omega_{pr} \psi_{rdq}^{+} \quad (15c)$$
$$\psi_{pdq}^{+} = L_p I_{pdq}^{+} + L_{pr} I_{rdq}^{+} \quad (15d)$$
$$\psi_{cdq}^{+} = L_c I_{cdq}^{+} - L_{cr} I_{rdq}^{+} \quad (15e)$$
$$\psi_{rdq}^{+} = L_r I_{rdq}^{+} + L_{pr} I_{pdq}^{+} - L_{cr} I_{cdq}^{+} \quad (15f)$$

RW power can be calculated as follows from (15d):

$$I_{rdq}^{+} = \frac{\psi_{pdq}^{+}}{L_{pr}} - \frac{L_p}{L_{pr}} I_{pdq}^{+} \quad (16)$$

What happens when you substitute (16) for (15e) and (15f)?

$$\psi_{rdq}^{+} = \frac{L_r}{L_{pr}} \psi_{pdq}^{+} - L_M I_{pdq}^{+} - L_{cr} I_{cdq}^{+} \quad (17)$$
$$\psi_{cdq}^{+} = L_c I_{cdq}^{+} - \frac{L_{cr}}{L_{pr}} \psi_{pdq}^{+} + \frac{L_{cr} L_p}{L_{pr}} I_{pdq}^{+} \quad (18)$$

By substituting (16) and (17) into (15c), RW voltage equation can be expressed as

$$V_{cdq}^{+} = R_c I_{cdq}^{+} + \sigma L_c p I_{cdq}^{+} + K_{cdq}^{+} \quad (20)$$

The leakage factor is σ = 1 − L2crLp/ (Lpr LM Lc), and K+cdq includes all d and q axes disturbances and cross-coupling variables.

$$K_{cdq}^{+} = (j\omega_c L_c - j\frac{\omega_{pr} L_{cr}^2 L_p}{L_{pr} L_M}) I_{cdq}^{+} + (j\frac{\omega_c L_{cr} L_p}{L_{pr}} - \frac{R_r L_p^2 L_{cr}}{L_{pr}^2 L_M} - j\frac{\omega_{pr} L_{cr} L_p}{L_{pr}}) I_{pdq}^{+} + (-j\frac{\omega_c L_{cr}}{L_{pr}} + \frac{R_r L_p L_{cr}}{L_{pr} L_M} + j\frac{\omega_{pr} L_{cr} L_p L_r}{L_{pr}^2 L_M}) \psi_{pdq}^{+} \quad (21)$$

$$I_{cdq}^{+} \approx \frac{L_r}{L_{pr} L_{cr}} \psi_{pdq}^{+} - \frac{L_M}{L_{cr}} I_{pdq}^{+} \quad (22)$$

You can compute the PW apparent Sp under grid voltage imbalance using the formulas [15], [16].

$$S_p = P_p + jQ_p = -\frac{3}{2} V_{pdq}^{+} \bar{I}_{pdq}^{+} \quad (23)$$

Combining equations (14), (22), and (23) separates power into oscillating and average components, both reactive and active.

$$P_p = P_{p0} + P_{ps2} \sin 2\omega_p t + P_{pc2} cos 2\omega_p t$$
$$Q_p = Q_{p0} + Q_{ps2} \sin 2\omega_p t + Q_{pc2} cos 2\omega_p t \quad (24)$$

Where Pp0, Qp0, Pps2, Ppc2, Qps2, and Qpc2 represent the oscillating and average parts of reactive and active power.

$$\begin{bmatrix} P_{p0} \\ Q_{p0} \\ P_{ps2} \\ P_{pc2} \\ Q_{ps2} \\ Q_{pc2} \end{bmatrix} = -\frac{3L_r}{2L_M L_{pr}} \begin{bmatrix} V_{pd+}^{+} & V_{pq+}^{+} & V_{pd-}^{-} & V_{pq-}^{-} \\ V_{pq+}^{+} & -V_{pd+}^{+} & V_{pq-}^{-} & -V_{pd-}^{-} \\ V_{pq-}^{-} & -V_{pd-}^{-} & -V_{pq+}^{+} & V_{pd+}^{+} \\ V_{pd-}^{-} & V_{pq-}^{-} & V_{pd+}^{+} & V_{pq+}^{+} \\ -V_{pd-}^{-} & -V_{pq-}^{-} & V_{pd+}^{+} & V_{pq+}^{+} \\ V_{pq-}^{-} & -V_{pd-}^{-} & V_{pq+}^{+} & -V_{pd+}^{+} \end{bmatrix} \begin{bmatrix} \psi_{pd+}^{+} \\ \psi_{pq+}^{+} \\ \psi_{pd-}^{-} \\ \psi_{pq-}^{-} \end{bmatrix} + \frac{3L_{cr}}{2L_M} \begin{bmatrix} V_{pd+}^{+} & V_{pq+}^{+} & V_{pd-}^{-} & V_{pq-}^{-} \\ V_{pq+}^{+} & -V_{pd+}^{+} & V_{pq-}^{-} & -V_{pd-}^{-} \\ V_{pq-}^{-} & -V_{pd-}^{-} & -V_{pq+}^{+} & V_{pd+}^{+} \\ V_{pd-}^{-} & V_{pq-}^{-} & V_{pd+}^{+} & V_{pq+}^{+} \\ -V_{pd-}^{-} & -V_{pq-}^{-} & V_{pd+}^{+} & V_{pq+}^{+} \\ V_{pq-}^{-} & -V_{pd-}^{-} & V_{pq+}^{+} & -V_{pd+}^{+} \end{bmatrix} \begin{bmatrix} I_{cd+}^{+} \\ I_{cq+}^{+} \\ I_{cd-}^{-} \\ I_{cq-}^{-} \end{bmatrix} \quad (25)$$

The electromagnetic force of BDFIG under unbalanced grid voltage is represented as [16].

$$T_{em} = \frac{3}{2} p_p im\left(\bar{\psi}_{pdq}^{+} I_{pdq}^{+}\right) + \frac{3}{2} p_c im\left(\psi_{cdq}^{+} \bar{I}_{cdq}^{+}\right) \quad (26)$$

Using (14) and substituting (18) and (22) into (26) yield

$$T_{em} = \frac{3}{2} p_p im\left(\bar{\psi}_{pdq}^{+} I_{pdq}^{+}\right) + \frac{3}{2} p_c im\left(\psi_{cdq}^{+} \bar{I}_{cdq}^{+}\right) = -\frac{3}{2} p_p \frac{L_{cr}}{L_M} im\left(\bar{\psi}_{pdq}^{+} I_{cdq}^{+}\right) + \frac{3}{2} p_c \left(\frac{L_{cr} L_p L_r}{L_M L_{pr}^2} - \frac{L_{cr}}{L_{pr}}\right) \times im\left(\psi_{pdq}^{+} \bar{I}_{cdq}^{+}\right) = T_{em0} + T_{ems2} \sin 2\omega_p t + T_{emc2} \cos 2\omega_p t \quad (27)$$

where Tem0, Tems2, and Temc2 represent the average torque and oscillating torque components' amplitudes of electromagnetic torque.

$$\begin{bmatrix} T_{em0} \\ T_{ems2} \\ T_{emc2} \end{bmatrix} = \lambda_{Tem} \begin{bmatrix} -\psi_{pq+}^{+} & \psi_{pd+}^{+} & -\psi_{pq-}^{-} & \psi_{pd-}^{-} \\ \psi_{pd-}^{-} & \psi_{pq-}^{-} & -\psi_{pd+}^{+} & -\psi_{pq+}^{+} \\ -\psi_{pq-}^{-} & \psi_{pd-}^{-} & -\psi_{pq+}^{+} & \psi_{pd+}^{+} \end{bmatrix} \begin{bmatrix} I_{cd+}^{+} \\ I_{cq+}^{+} \\ I_{cd-}^{-} \\ I_{cq-}^{-} \end{bmatrix} \quad (28)$$

$$\lambda_{Tem} = \frac{3}{2} \left(\frac{p_c L_{cr} L_p L_r}{L_M L_{pr}^2} - \frac{p_c L_{cr}}{L_{pr}} - \frac{p_p L_{cr}}{L_M}\right) \quad (29)$$

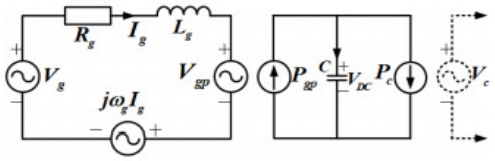

FIGURE 5. Equivalent circuit of a GSC in dq reference frame.

(B). The grid voltage imbalance vectors model of gsc:

Figure 5 presents the GSC's equivalent circuit in the dq reference frame, modeled with an angular speed of ωp, as per [18].

$$V_g = R_g I_g + L_g p I_g + j\omega_p L_g I_g + V_{gp} \quad (30)$$
$$C\frac{dV_{dc}}{dt} \cdot V_{dc} = P_{gp} - P_c \quad (31)$$

Given Fig. 4, Both positive and negative sequencing elements in the (dgqg)+ or (dgqg)- frames of reference can be used to characterise vector F under grid voltage imbalance.

$$\begin{aligned} F^{+}_{gdq} &= F^{+}_{gdq+} + F^{-}_{gdq-}e^{-j2\omega_p t} \\ F^{-}_{gdq} &= F^{-}_{gdq-} + F^{+}_{gdq+}e^{j2\omega_p t} \end{aligned} \quad (32)$$

GSC power in the (dgqg)+ frames is obtained under a grid voltage imbalance by replacing (32) into (30).

$$V^{+}_{gdq} = R_g I^{+}_{gdq} + L_g p I^{+}_{gdq} + j\omega_p L_g I^{+}_{gdq} + V^{+}_{gpdq} \quad (33)$$

Likewise, under grid voltage unbalance, the input apparent power Sg of GSC can be calculated as

$$S_g = P_g + jQ_g = -\frac{3}{2}V^{+}_{gdq}\bar{I}^{+}_{gdq} \quad (34)$$

Using equation (32), substituting variations in voltage and current into (34), separates average and oscillating active/reactive power components.

$$\begin{aligned} P_g &= P_{g0} + P_{gs2}sin2\omega_p t + P_{gc2}\cos 2\omega_p t \\ Q_g &= Q_{g0} + Q_{gs2}sin2\omega_p t + Q_{gc2}\cos 2\omega_p t \end{aligned} \quad (35)$$

These terms represent average and oscillating parts of Power system analysis of both reactive and active power components.

$$\begin{bmatrix} P_{g0} \\ Q_{g0} \\ P_{gs2} \\ P_{gc2} \\ Q_{gs2} \\ Q_{gc2} \end{bmatrix} = -\frac{3}{2}\begin{bmatrix} V^{+}_{gd+} & V^{+}_{gq+} & V^{-}_{gd-} & V^{-}_{gq-} \\ V^{+}_{gq+} & -V^{+}_{gd+} & V^{-}_{gq-} & -V^{-}_{gd-} \\ V^{-}_{gq-} & -V^{-}_{gd-} & -V^{+}_{gq+} & V^{+}_{gd+} \\ V^{-}_{gd-} & V^{-}_{gq-} & V^{+}_{gd+} & V^{+}_{gq+} \\ -V^{-}_{gd-} & -V^{-}_{gq-} & V^{+}_{gd+} & V^{+}_{gq+} \\ V^{-}_{gq-} & -V^{-}_{gd-} & V^{+}_{gq+} & -V^{+}_{gd+} \end{bmatrix}\begin{bmatrix} I^{+}_{gd+} \\ I^{+}_{gq+} \\ I^{-}_{gd-} \\ I^{-}_{gq-} \end{bmatrix} \quad (36)$$

IV. Present standard deviations for msc and gsc have been calculated, together with a coordinated control approach and control objectives..

(A) machine side controller:

$$\begin{aligned} V^{+}_{pdq+} &= V^{+}_{pd+} + jV^{+}_{pq+} = V^{+}_{pd+} \approx j\omega_p \psi^{+}_{pdq+} \\ V^{-}_{pdq-} &= V^{-}_{pd-} + jV^{-}_{pq-} \approx -j\omega_p \psi^{-}_{pdq-} \end{aligned} \quad (37)$$

$$\begin{cases} I^{+*}_{cd+} = \dfrac{2L_M V^{+}_{pd+} P^{*}_{p0}}{3L_{cr}\left(V^{+2}_{pd+} + V^{-2}_{pd-} + V^{-2}_{pq-}\right)} \\ I^{+*}_{cq+} = -\dfrac{2L_M V^{+}_{pd+} Q^{*}_{p0}}{3L_{cr}\left(V^{+2}_{pd+} - V^{-2}_{pd-} - V^{-2}_{pq-}\right)} - \dfrac{L_r V^{+}_{pd+}}{L_{pr}L_{cr}\omega_p} \\ I^{-*}_{cd-} = \dfrac{V^{-}_{pd-}}{V^{+}_{pd+}} I^{+*}_{cd+} + \dfrac{V^{-}_{pq-}}{V^{+}_{pd+}} I^{+*}_{cq+} \\ I^{-*}_{cq-} = \dfrac{V^{-}_{pq-}}{V^{+}_{pd+}} I^{+*}_{cd+} - \dfrac{V^{-}_{pd-}}{V^{+}_{pd+}} I^{+*}_{cq+} \end{cases} \quad (38)$$

(B) gride side controller:

$$\bar{I}^{-}_{p\alpha\beta-} + \bar{I}^{-}_{g\alpha\beta-} = \bar{I}^{-}_{pdq-}e^{-j\omega_p t} + \bar{I}^{-}_{gdq-}e^{-j\omega_p t} = 0 \quad (39)$$

$$\begin{cases} I^{+*}_{gd+} = \dfrac{-2P^{*}_{g0}}{3V^{+}_{gd+}} + \dfrac{V^{-}_{gd-}}{V^{+}_{gd+}} I^{-}_{pd-} + \dfrac{V^{-}_{gq-}}{V^{+}_{gd+}} I^{-}_{pq-} \\ I^{+*}_{gq+} = \dfrac{2Q^{*}_{g0}}{3V^{+}_{gd+}} - \dfrac{V^{-}_{gq-}}{V^{+}_{gd+}} I^{-}_{pd-} + \dfrac{V^{-}_{gd-}}{V^{+}_{gd+}} I^{-}_{pq-} \\ I^{-*}_{gd-} = -I^{-}_{pd-} \\ I^{-*}_{gq-} = -I^{-}_{pq-} \end{cases} \quad (40)$$

According to equations (24) and (35), the total amount of active power (Ptotal) for Objective II, as shown in Fig. 1, is the product of the active power output from the BDFIG PW plus the GSC.

$$\begin{aligned} P_{total} = &\left(P_{p0} + P_{g0}\right) + \left(P_{ps2} + P_{gs2}\right)\sin 2\omega_p t \\ &+ \left(P_{pc2} + P_{gc2}\right)\cos 2\omega_p t \end{aligned} \quad (41)$$

$$\begin{cases} I^{+*}_{gd+} = \dfrac{-2\left(V^{+}_{gd+}P^{*}_{g0} + V^{-}_{gd-}P_{pc2} + V^{-}_{gq-}P_{ps2}\right)}{3\left(V^{+2}_{gd+} - V^{-2}_{gd-} - V^{-2}_{gq-}\right)} \\ I^{+*}_{gq+} = \dfrac{2\left(V^{+}_{gd+}Q^{*}_{g0} - V^{-}_{gd-}P_{ps2} + V^{-}_{gq-}P_{pc2}\right)}{3\left(V^{+2}_{gd+} + V^{-2}_{gd-} + V^{-2}_{gq-}\right)} \\ I^{-*}_{gd-} = \dfrac{2P_{pc2}}{3V^{+}_{gd+}} - \dfrac{V^{-}_{gd-}}{V^{+}_{gd+}} I^{+*}_{gd+} - \dfrac{V^{-}_{gq-}}{V^{+}_{gd+}} I^{+*}_{gq+} \\ I^{-*}_{gq-} = \dfrac{2P_{ps2}}{3V^{+}_{gd+}} - \dfrac{V^{-}_{gq-}}{V^{+}_{gd+}} I^{+*}_{gd+} + \dfrac{V^{-}_{gd-}}{V^{+}_{gd+}} I^{+*}_{gq+} \end{cases} \quad (43)$$

Objective III states that in Figure 1, the total reactive power \(Q-{\text{total}} \) is the sum of \(Q_p \) and \(Q_g \). To prevent oscillations in PW reactive power and BDFIG electromagnetic torque, \(Q_{ps2} = 0 \) and \(Q_{pc2} = 0 \), are both controlled. In order to remove oscillations in the overall reactive power output, it is also necessary to satisfy \(Q_{gs2} = 0 \) and \(Q_{gc2} = 0 \). Therefore, according to equation (36),

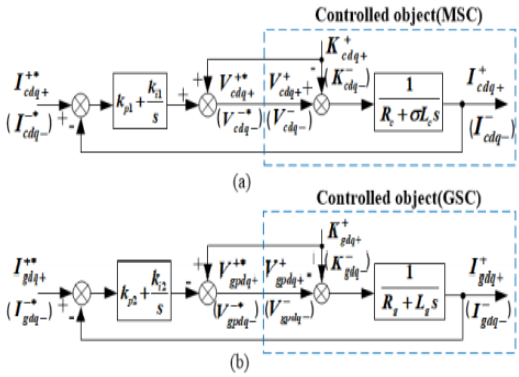

Figure 6. Present controllers in the reference frames (dq) + and (dq) −. (A) Current Controller for MSC. Current controller for GSC (b). One can determine the necessary references for GSC currents as

$$\begin{cases} I_{gd+}^{+*} = \dfrac{-2V_{gd+}^{+}P_{g0}^{*}}{3\left(V_{gd+}^{+2}+V_{gd-}^{-2}+V_{gq-}^{-2}\right)} \\ I_{gq+}^{+*} = \dfrac{2V_{gd+}^{+}Q_{g0}^{*}}{3\left(V_{gd+}^{+2}-V_{gd-}^{-2}-V_{gq-}^{-2}\right)} \\ I_{gd-}^{-*} = \dfrac{V_{gd-}}{V_{gd+}^{+}}I_{gd+}^{+*} + \dfrac{V_{gq-}^{-}}{V_{gd+}^{+}}I_{gq+}^{+*} \\ I_{gq-}^{-*} = \dfrac{V_{gq-}^{-}}{V_{gd+}^{+}}I_{gd+}^{+*} - \dfrac{V_{gd-}^{-}}{V_{gd+}^{+}}I_{gq+}^{+*} \end{cases} \quad (44)$$

For coordinated control, MSC and GSC must follow their reference currents for both positive and negative sequences.

1) MSC (BDFIG) current controller First, calculate \(I^*_{cd+} \), \(I^*_{cq+} \), \(I^*_{cd-} \), and \(I^*_{cq-} \) from \(P^*_{p0} \), \(Q^*_{p0} \), and equation (38). Then design the current controller using equations (14) and (20).

$$V_{cdq+}^{+*} = k_{p1}(I_{cdq+}^{+*} - I_{cdq+}^{+}) + k_{i1}\int (I_{cdq+}^{+*} - I_{cdq+}^{+}) + K_{cdq+}^{+} \quad (45)$$

$$V_{cdq-}^{-*} = k_{p1}(I_{cdq-}^{-*} - I_{cdq-}^{-}) + k_{i1}\int (I_{cdq-}^{-*} - I_{cdq-}^{-}) + K_{cdq-}^{-} \quad (46)$$

$$V_{c\alpha\beta}^{*} = V_{cdq+}^{+*}e^{j[\theta_p-(p_p+p_c)\theta_r]} + V_{cdq-}^{-*}e^{-j[\theta_p-(p_p+p_c)\theta_r]} \quad (47)$$

2) Current controller for GSC. Based on equations P ∗ g0, Q ∗ g0, (40), (43), and (44), the variables I +∗ gd+, I +∗ gq+, I −∗ gd−, and I −∗ gq− can be found. Using (32) and (33), GSC current controllers for (dgqg) + and (dgqg) − reference frames are designed with decoupling and feedback control.

$$V_{gpdq+}^{+*} = -\left[k_{p2}(I_{gdq+}^{+*} - I_{gdq+}^{+}) + k_{i2}\int (I_{gdq+}^{+*} - I_{gdq+}^{+})\right] + K_{gdq+}^{+} \quad (48)$$

$$V_{gpdq-}^{-*} = -\left[k_{p2}(I_{gdq-}^{-*} - I_{gdq-}^{-}) + k_{i2}\int (I_{gdq-}^{-*} - I_{gdq-}^{-})\right] + K_{gdq-}^{-} \quad (49)$$

$$\begin{cases} K_{gdq+}^{+} = V_{gdq+}^{+} + j\omega_p L_g I_{gdq+}^{+} \\ K_{gdq-}^{-} = V_{gdq-}^{-} - j\omega_p L_g I_{gdq-}^{-} \end{cases} \quad (50)$$

The General Services Commission current control diagram is shown in Fig. 6(b) based on equations (48) and (49). In the (αgβg) citation frame, the total GSC control voltage combines outputs from positive and negative sequence current controllers, as shown in Fig. 4.

$$V_{gp\alpha\beta}^{*} = V_{gpdq+}^{+*}e^{j\theta_g} + V_{gpdq-}^{-*}e^{-j\theta_g} \quad (51)$$

To successfully regulate the good and negative sequence, use the MSC and GSC control designs shown above..

V. Proposed Predictive Control Models

Chemical plants and other businesses use Model Predictive Control (MPC), an advanced control technique. power systems. Unlike PID and LQR controllers, MPC optimizes current actions while considering future impacts. It uses dynamic models, typically linear and empirical, to predict future events and adjust controls accordingly. MPC operates over a set time-horizon, applying only the immediate action, and is usually implemented digitally, though faster analog versions are being explored.

- **Principles of MPC:**

The multivariable control algorithm known as Model Predictive Control (MPC) makes use of:

- an internal dynamic process model
- an optimisation cost function J across the fading prediction horizon, and a history of previous control actions,

to determine the best control movements. Here is an illustration of an irregular cost function for optimisation::

$$J = \sum_{i=1}^{N} w_{x_i}(r_i - x_i)^2 + \sum_{i=1}^{N} w_{u_i}\Delta u_i^2$$

Without violating constraints (low/high limits) With:

x_i = i -th controlled variable (e.g. measured temperature)

r_i = i -th reference variable (e.g. required temperature)

u_i = i -th manipulated variable (e.g. control valve)

w_{x_i} = weighting coefficient reflecting the relative importance of x_i

w_{u_i} = weighting coefficient penalizing relative big changes in u_i

- **Robust MPC:**

- Min-max MPC optimizes against all potential disturbances, offering robust control but at high cost of calculation.
- Strict Restrictions State limitations are expanded by MPC. to ensure a feasible trajectory despite disturbances.
- Tube MPC uses a model and feedback control to keep the actual state close to the desired state, maintaining a safe distance determined using the sturdy positive invariant (RPI) set.
- A situation-tree is used in multi-stage MPC. to handle uncertainties, adapting decisions at each stage based on new data. It's efficient but becomes impractically large with more uncertainties and longer prediction horizons.

- **Multilevel inverter**

Multilevel converters, pioneered in 1975, initially used a three-level design and have since evolved with various topologies. They employ multiple lower voltage DC sources, like capacitors or batteries, to create higher power outputs by combining these sources through power switches. Each switch's voltage rating matches its connected DC source. This allows for efficient power conversion using staircase voltage waveforms.

Multilevel inverters come in a few varieties.

(a)Cascaded H Bridge Inverters

(b)Diode Clamped Inverters

(c)Flying Capacitor Inverters

(a) multi-level cascading H bridge Inverters:

Multiple independent DC sources (SDCS) are used by an inverter seen in Figure (a) to generate AC output. A a single-phase full-bridge or the H-bridge inverter receives connections from each source. By alternating permutations of four switch (S1, S2, S3, S4), these inverters can provide three outputs: +Vdc, 0Vdc, and –Vdc. Switch S1 and S4 are used for +Vdc, for instance, whereas –Vdc
uses S2 and S3. When all switches are off, the output is 0. Multiple Inverter levels have a series connection. to synthesize a complex waveform, like the one shown in Figure (b). Using m = 2s+1, where s is the amount of DC sources, one may calculate that amount of output voltage levels, m.

$$H(n)=\frac{4}{\pi n}\left[\cos(n\theta_1)+\cos(n\theta_2)+\ldots+\cos(n\theta_s)\right],\quad \text{where } n=1,3,5,7,\ldots$$

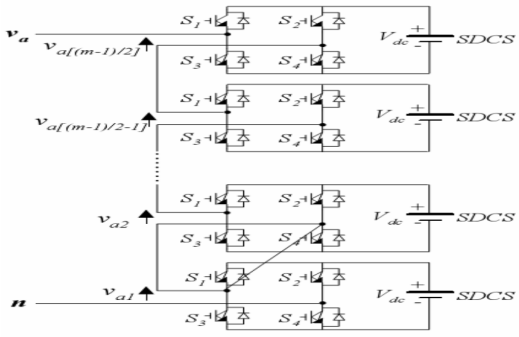

Fig:7(a). Single-phase structure of a cascaded H-bridges inverter

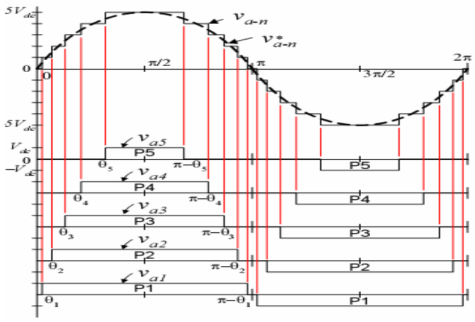

Fig:7(b). Output phase voltage waveform of an 11-level cascade inverter with 5 separate dc sources.

Conducting angles 1, 2, 3 are selected to minimize voltage distortion by eliminating lower frequency harmonics: 5th, 7th, 11th,

VI. Multiple-level inverter control and modulation methods:

Segmentation of Signal Processing Techniques:

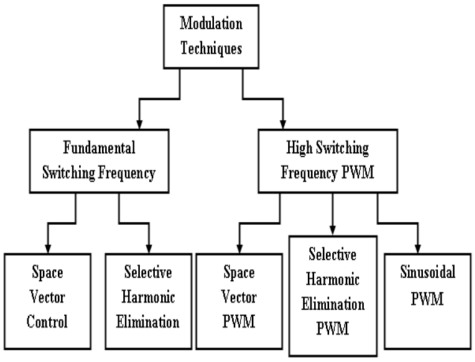

VI(a). Classifications of Multilevel Modulation Methods:

In industrial applications, high-frequency Sinusoidal PWM (SPWM) with phase-shifting is widely used. Selective harmonic elimination, multilevel space vector PWM, and multilevel carrier-based PWM are the three primary multilevel modulation techniques., extending traditional two-level strategies.

VI(b). Multilevel SPWM

Multilevel SPWM uses various carriers, and several methods reduce distortion in multilevel inverters using triangular wave-based SPWM.

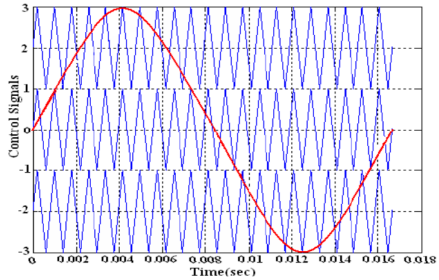

(a)

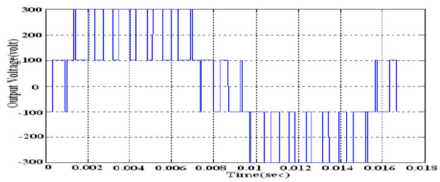

(b)

Fig:8. Control and carrier signals are part of multi-carrier control; output voltage is part of it.

By employing a single reference signal in comparison to carriers, the Multilevel SPWM technique expands upon the bi-level SPWM.. The converter cell produces positive voltage when the reference is greater and negative voltage when it is not. Using three series cells in each phase of a seven-level inverter, minimal distortion occurs with carriers shifted by 120°.

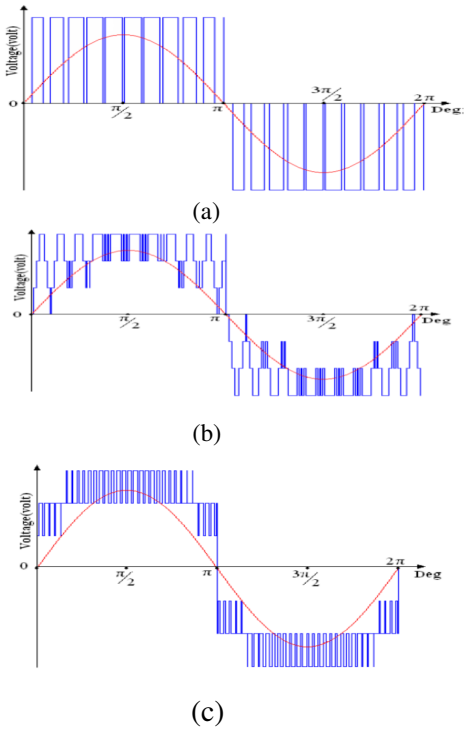

Diagram 9. Output Voltages Including Carriers Phase shift: 0°, 90°, and 120° are the possible values.

VI (C). Space Vector Modulation (SVM):

The SVM method is adaptable for multilevel inverters, illustrated by Vector diagrams in space for inverters with three, four, and seven levels.

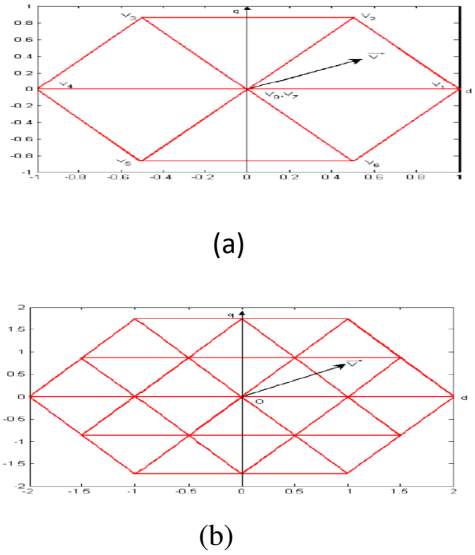

Figure:10 Space Vector Diagram (a)Three-Level; (b) Five-Level

VII.CASE STUDIES

Case studies are completed in Matlab-Simulink for a 2 Megawatt BDFIG-based turbine system. Table 2 lists the BDFIG parameters.. A transition between the Scm and GSC occurs at 2.55 kHz, and the General Services Commission cutoff Lg is 0.16 mH. By employing the voltage unbalance factor, voltage imbalance may be calculated.

$$\varepsilon = \frac{V_{g-}}{V_{g+}} \times 100\% \qquad (52)$$

TABLE 2. Parameters of 2WM BDFIG system.

Rated power	2MW
RatedPW voltage	690v
Rated PWfrequency	50HZ
R_p, R_c, R_r (Ω)	0.0012,0.0072,0.0010
L_p, L_c, L_{cr} (mH)	3.1000,6.8890,19.050
L_{pr} L_{cr} (mH)	6.6560,4.8940
$P_{p,,}P_c$	2,2

where $V_{g-}$and V_{g+} symbolise, respectively, the grid of the power vector's both positive and negative sequencing components.

$V_{g-}=(V_{ga}+a^2V_{gb}+aV_{gc})/3$, $V_{g+}=(V_{ga}+aV_{gb}+a^2V_{gc})$ /3, $a1/2j$ 3/2, V_{ga}, V_{gb} and V_{gc} represent three phase grid voltage vector.

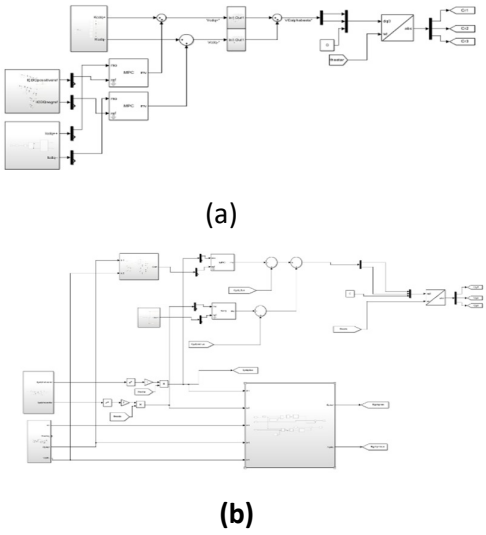

FIGURE:10. Simulation diagram of MPC, for(a) MSC and(b) GSC.

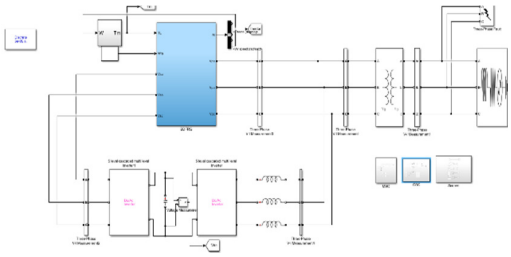

FIGURE:11. Simulation Figure showing the suggested MPC coordinated control for MSC and GSC in the BDFIG generation system.

VIII.COMPARISON OF SIMULATION RESULTS:

I.CASE: Fast Sequence decomposition algorithm.

PI controller results:

MPC controller results:

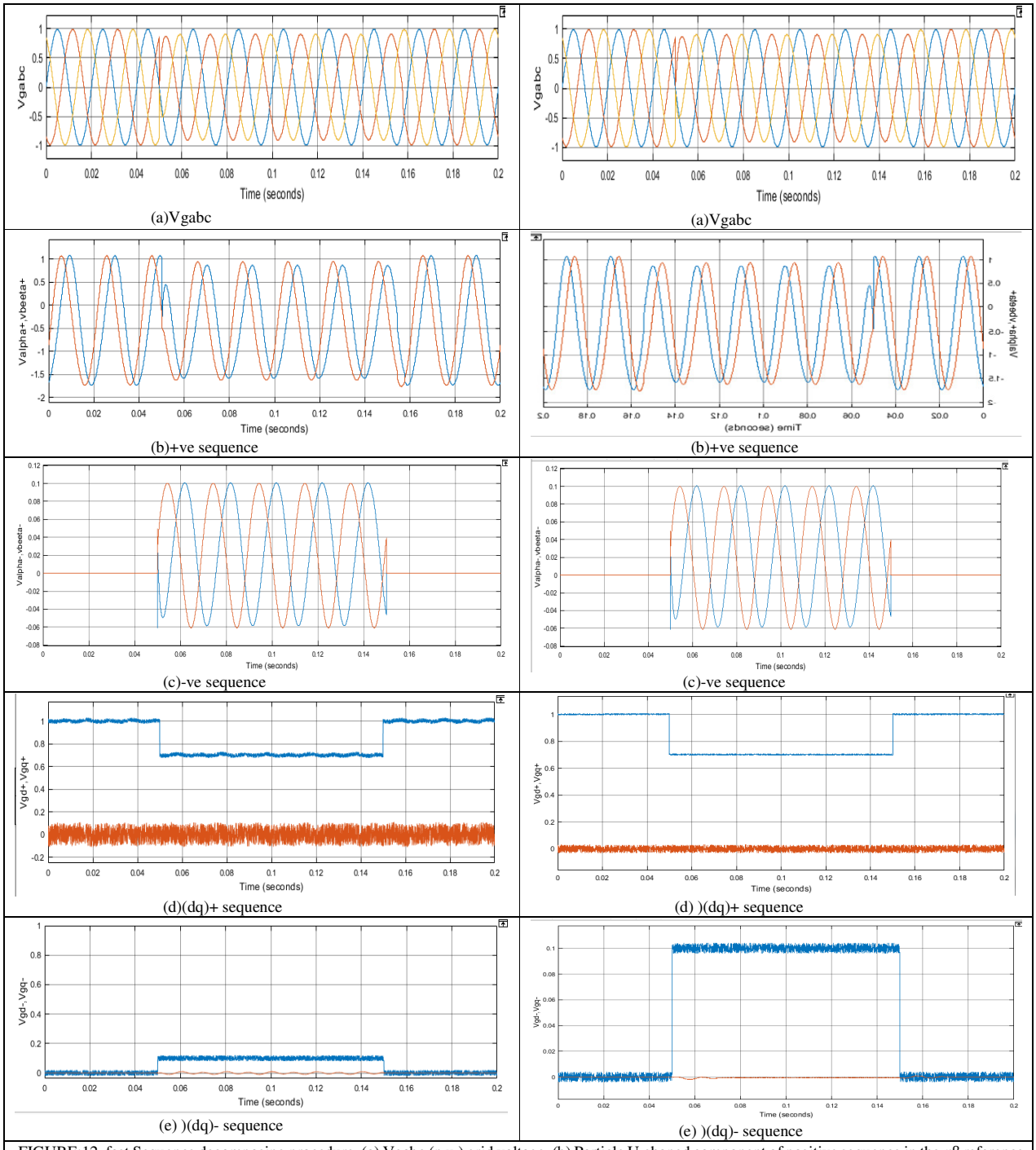

(a)Vgabc (a)Vgabc

(b)+ve sequence (b)+ve sequence

(c)-ve sequence (c)-ve sequence

(d)(dq)+ sequence (d))(dq)+ sequence

(e))(dq)- sequence (e))(dq)- sequence

FIGURE:12. fast Sequence decomposing procedure. (a) Vgabc (p.u.) grid voltage. (b) Particle U-shaped component of positive sequence in the αβ reference frame (c) In the αβ reference frame (p.u.), the negative sequence component. (d) Positive sequence element within the reference frame (p.u.)+(dq). (e) The negative sequence element within the (dq)– referencing frame (p.u.). Rapid breakdown of sequences algorithm using of PI controller (B) Fast sequence decomposition algorithm using of MPC controller.

II.CASE: Waveforms under 10% the electrical grid imbalance with three configurable control targets and the removal of torque oscillations.

PI controller results:

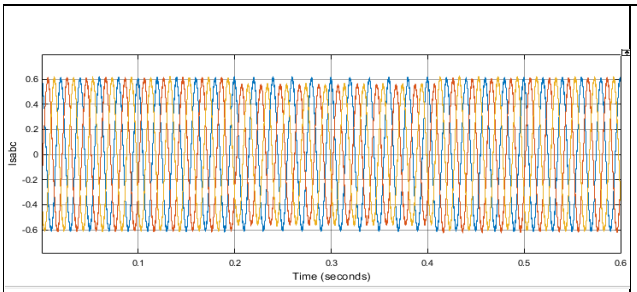

(a)Total output current

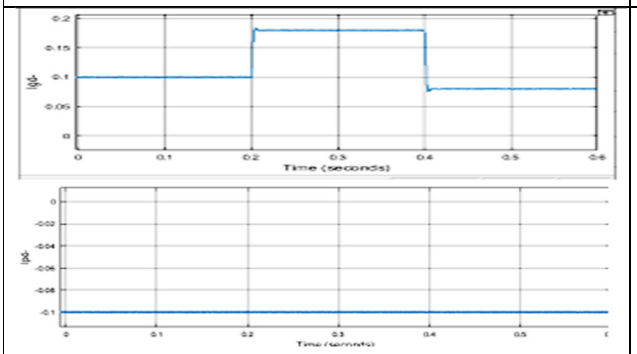

(b)GSC d-axis

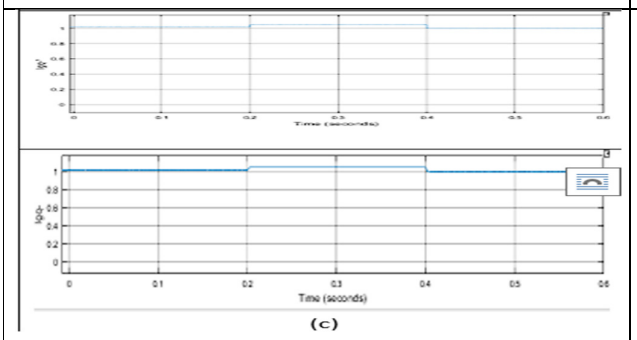

(c)PW q-axis

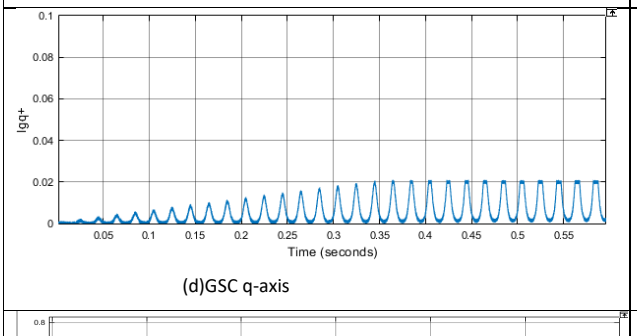

(d)GSC q-axis

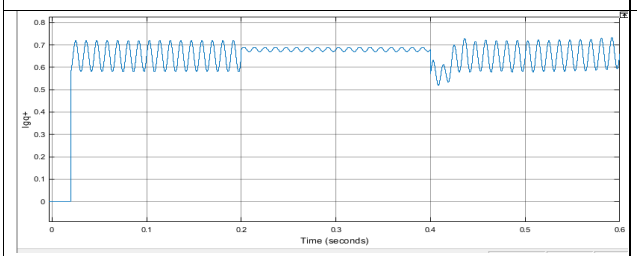

(e)GSC dc-axis

MPC controller results:

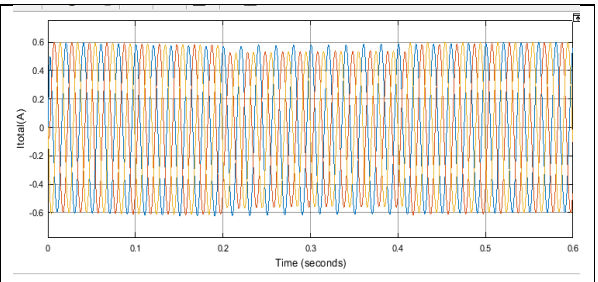

(a) Total output current

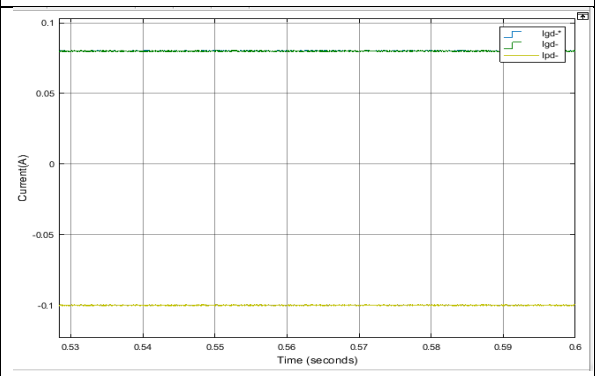

(b) GSC d-axis

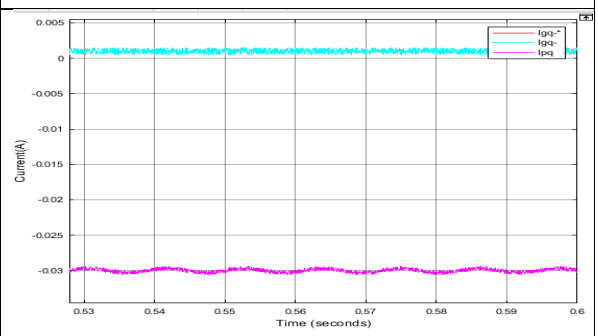

(c) PW q-axis

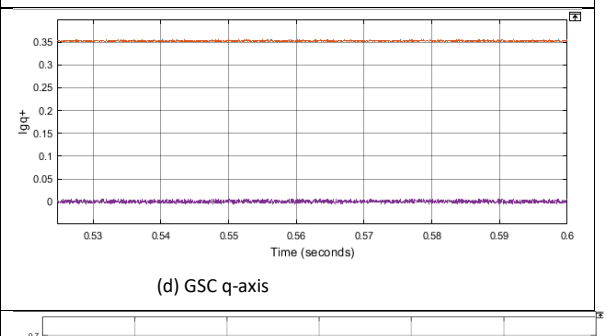

(d) GSC q-axis

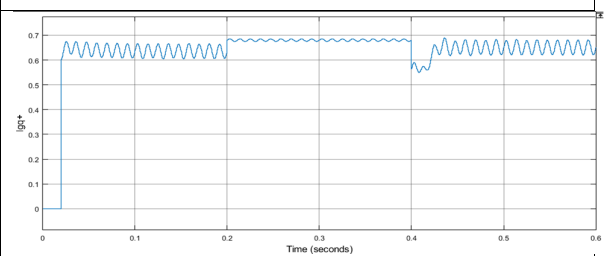

(e) GSC dc-axis

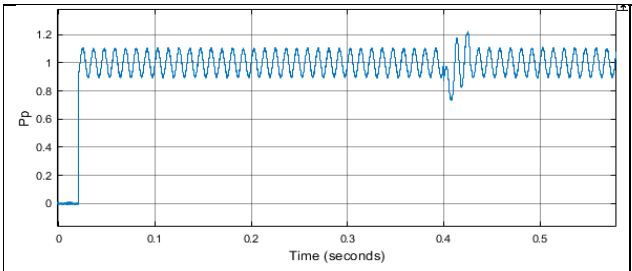

(f)Total output active power

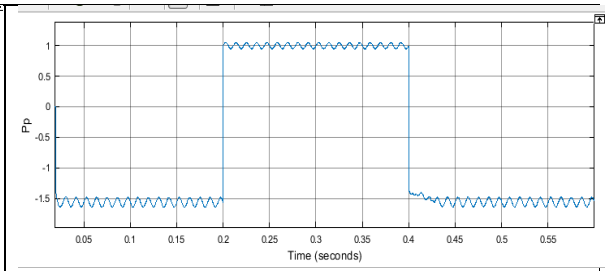

(f) Total output active power

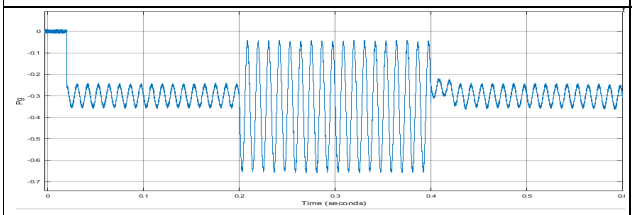

(g)PW and GSC active power

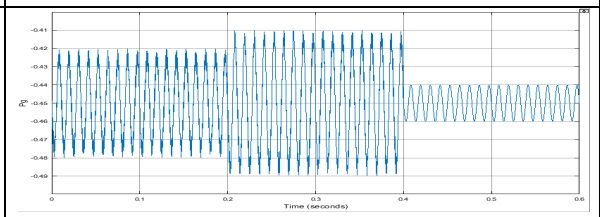

(g) PW and GSC active power

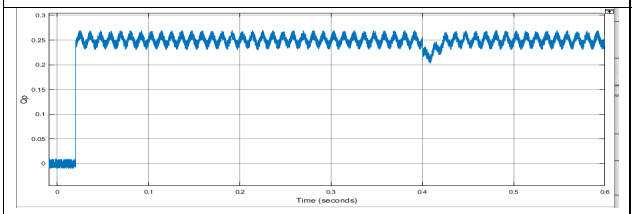

(h)Total reactive power

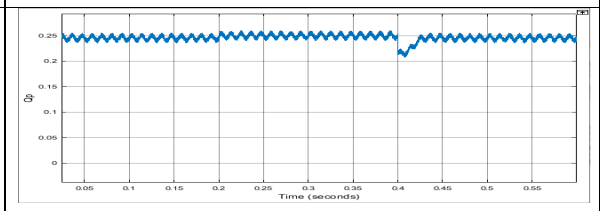

(h) Total reactive power

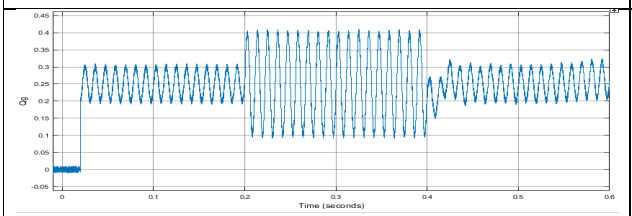

(i)PW andGSC reactive power

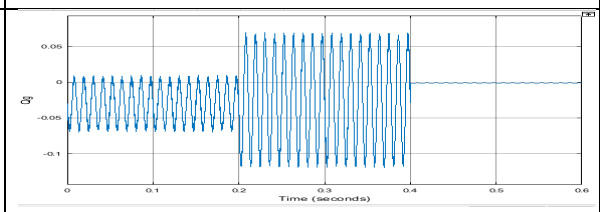

(i) PW andGSC reactive power

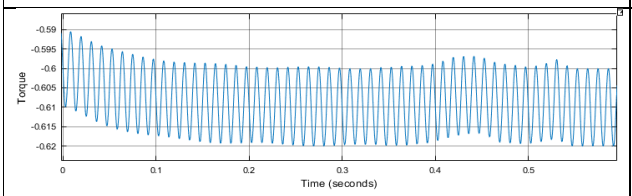

(j)Electromagnetic torque

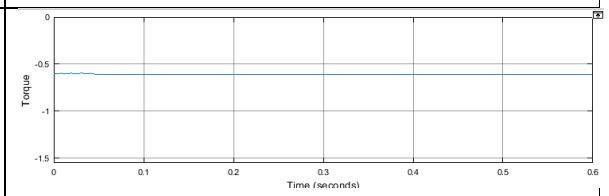

(j) Electromagnetic torque

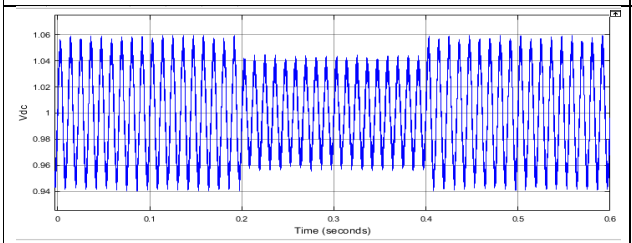

(k)DC link voltage

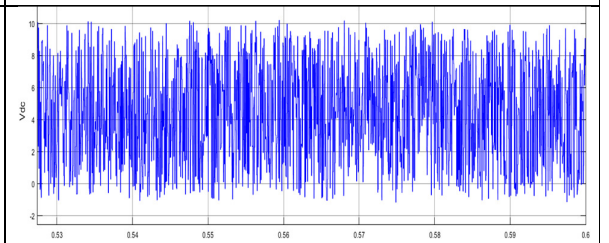

(k) DC link voltage

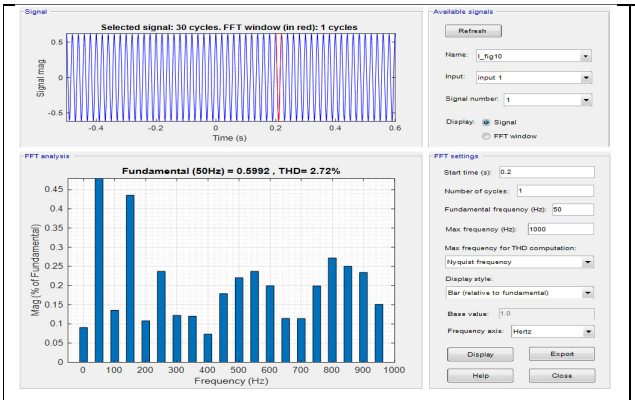

(I)THD value

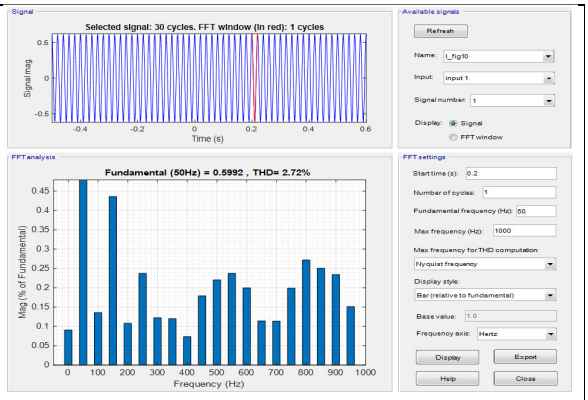

(I) THD value

FIGURE:13. Waveforms with elimination of torque oscillations and three selectable control objectives under 10% grid voltage unbalance (!r D 0:7 p.u., " D 10%). (a) Total output current (p.u.). (b) GSC d- axis(p.u.). (c) PW q- axis currents (p.u.). (d) GSC q- axis and PW d-axis currents (p.u.). (e) GSC dC axis and qC axis currents (p.u.). (f)Total output active power (p.u.). (g) PW and GSC active power (p.u.). (h) Total output reactive power (p.u.). (i) PW and GSC reactive power (p.u.). (j) Electromagnetic torque (p.u.). (k) DC link voltage (p.u.).(l)THD value (p.u.).

III.CASE**: Waveforms with two control modes under " Grid voltage of D 10%.**

PI controller results:

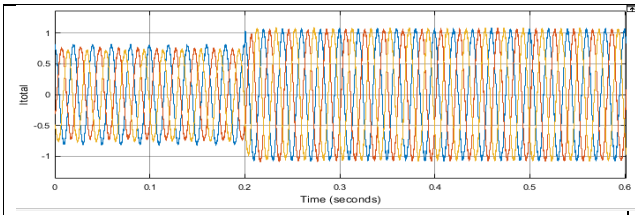

(a)Total output current

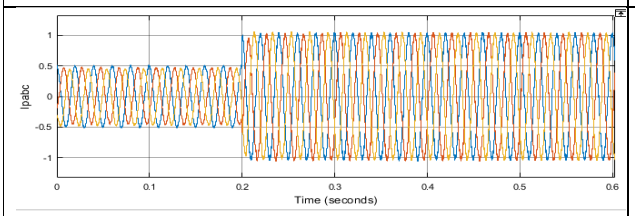

(b)PW voltage

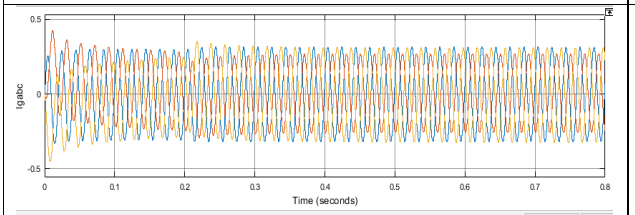

(c)GSC current

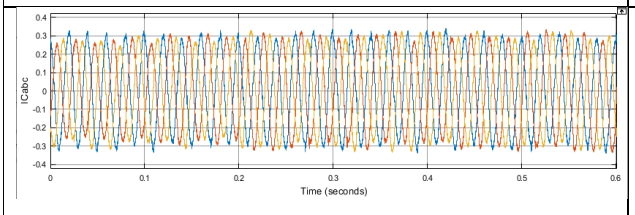

(d)CW current

MPC controller results:

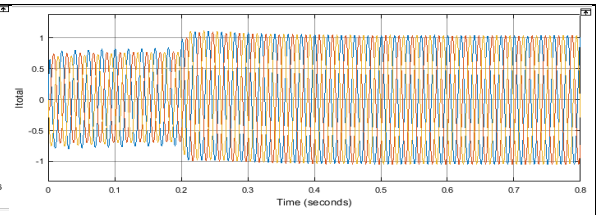

(a)Total output current

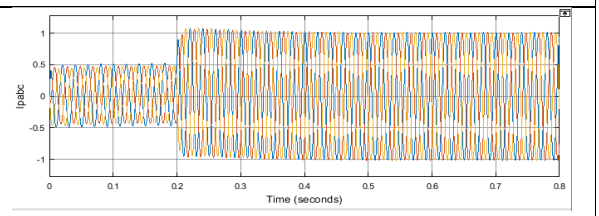

(b) PW voltage

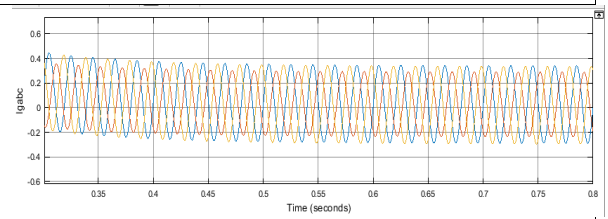

(c) GSC current

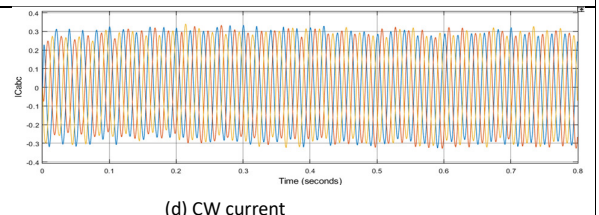

(d) CW current

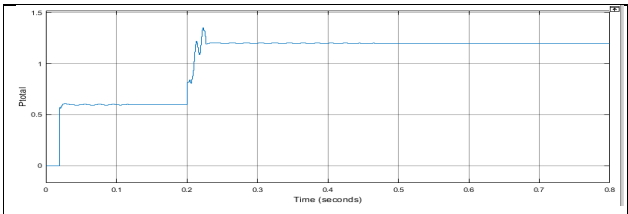

(e)Total output active power

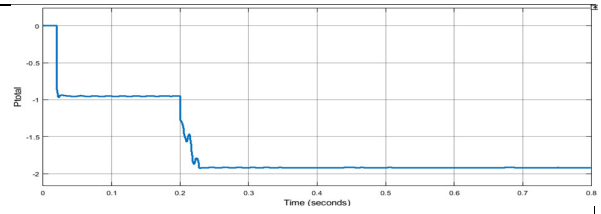

(e) Total output active power

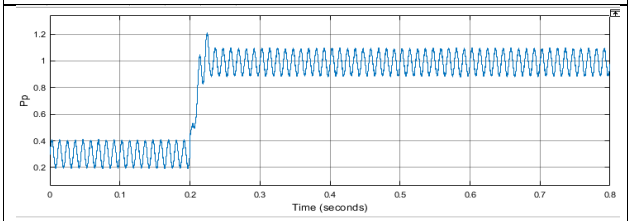

(f)PWactive power

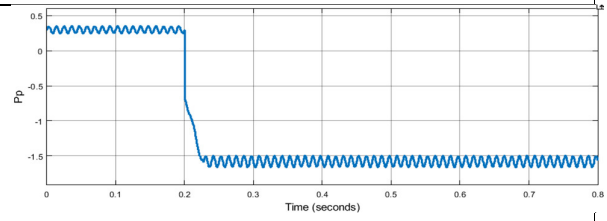

(f)PWactive power

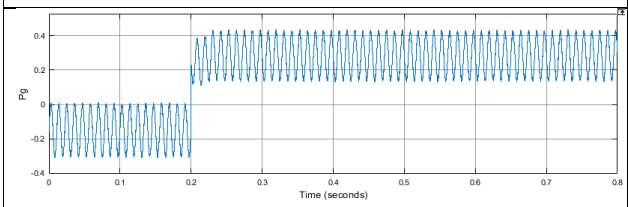

(g)GSC active power

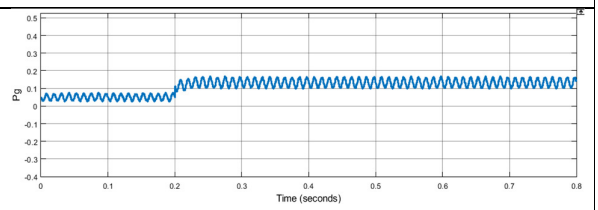

(g)GSC active power

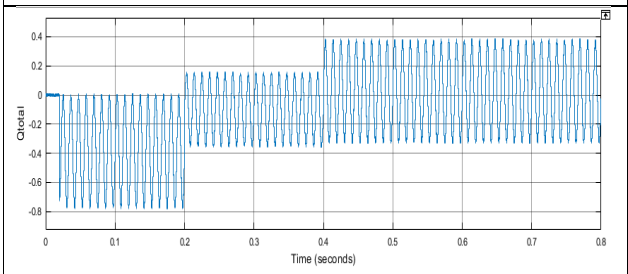

(h) Total output active power

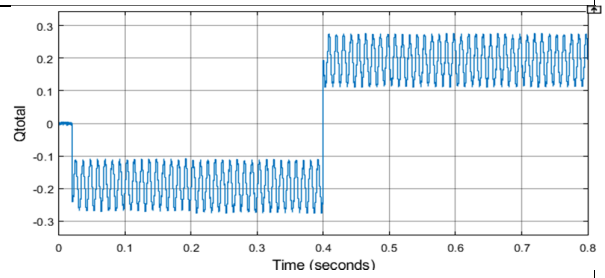

(h) Total output active power

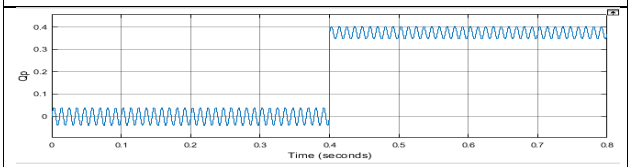

(i)PW reactive power

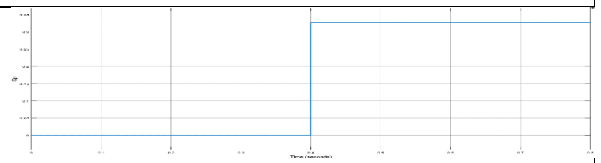

(i)PW reactive power

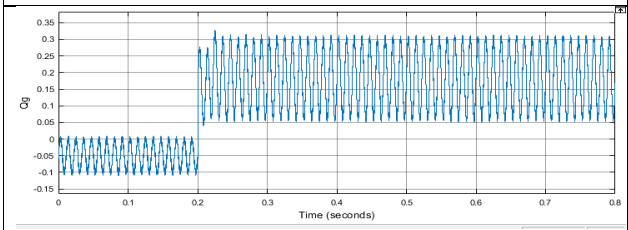

(j)GSC reactive power

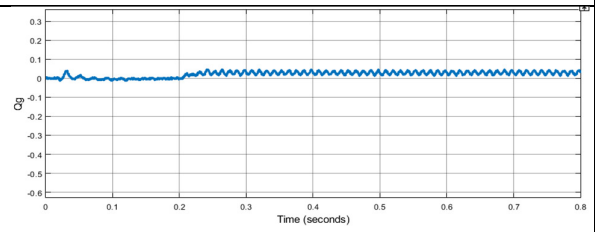

(j) GSC reactive power

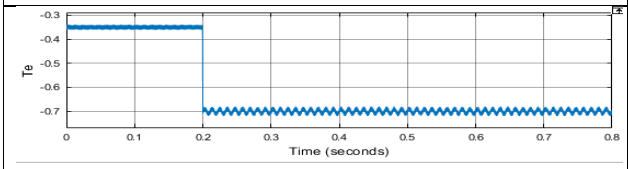

(k)Torque

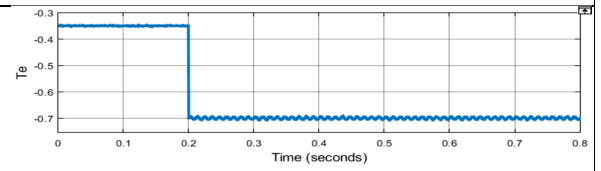

(k)Torque

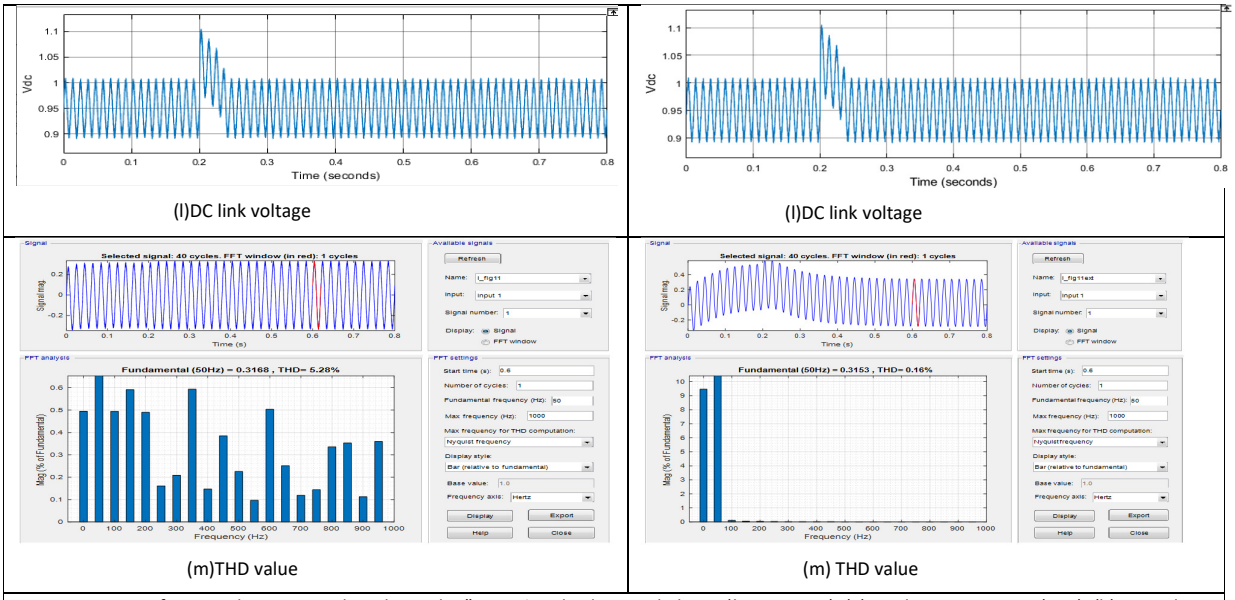

(l)DC link voltage (l)DC link voltage

(m)THD value (m) THD value

FIGURE:14. Waveforms with two control modes under " D 10% grid voltage unbalance (!r D 1:2 p.u.). (a) total output current (p.u.). (b) PW voltage (p.u.). (c) GSC current (p.u.). (d) CW current (p.u.). (e) Total output active power (p.u.). PW (f) active power(p.u.). (g) GSC active power (p.u.). (h) Total output reactive power (p.u.). (i) PW reactive power(p.u.).(j) GSC reactive power (p.u.). (k) BDFIG electromagnetic torque (p.u.). (l) DC link voltage. (m)THD value(p.u.).

IV.CASE: **Waveforms with variation of rotating speed under " D 10% uneven grid voltage.**

PI controller results: **MPC** controller results:

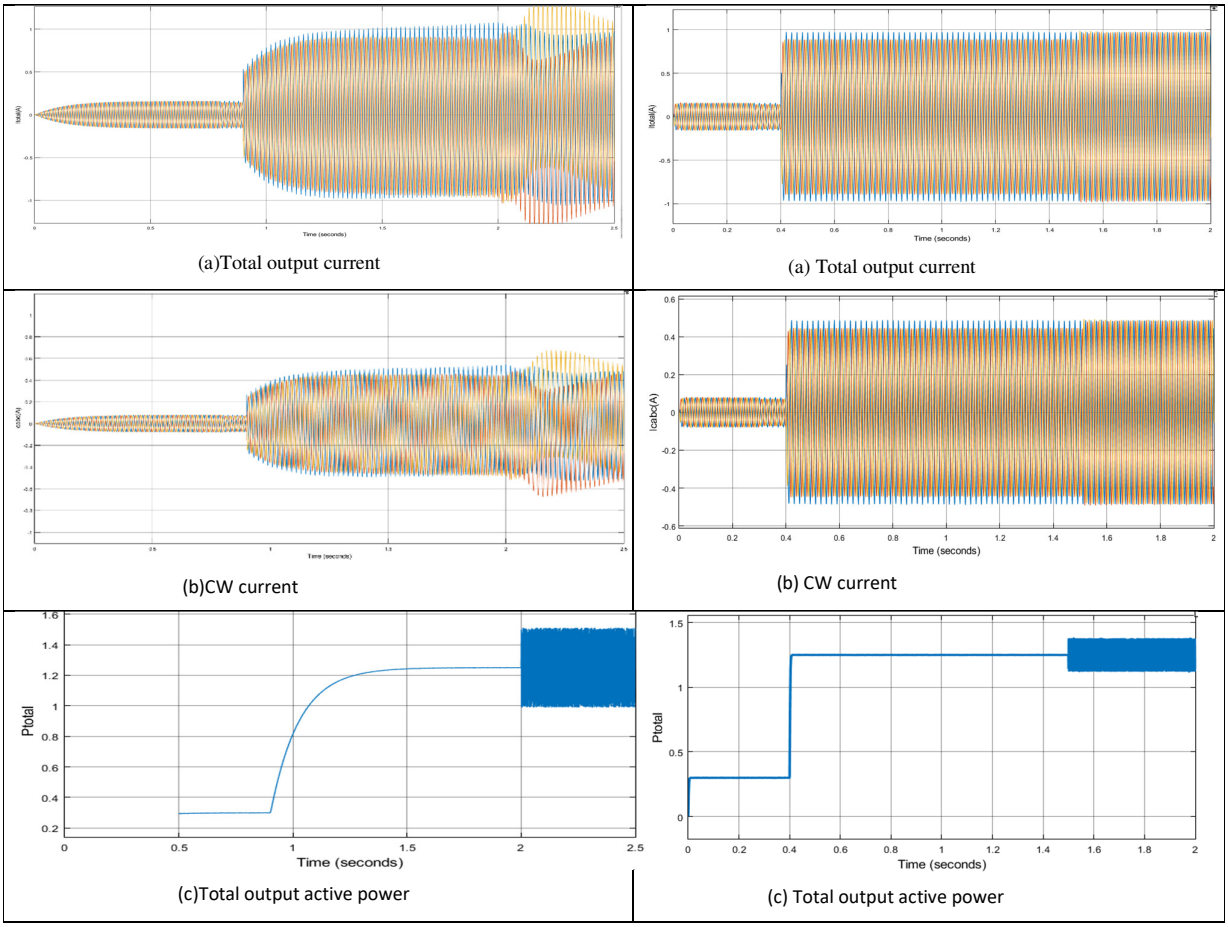

(a)Total output current (a) Total output current

(b)CW current (b) CW current

(c)Total output active power (c) Total output active power

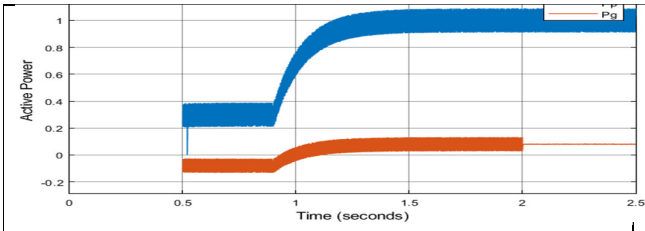

(d)PW and GSC active power

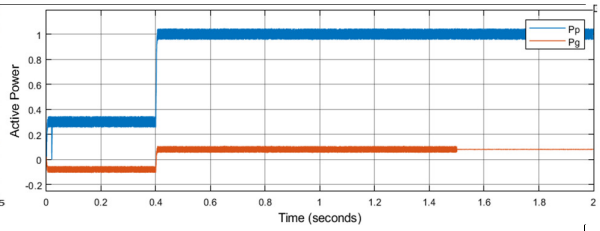

(d) PW and GSC active power

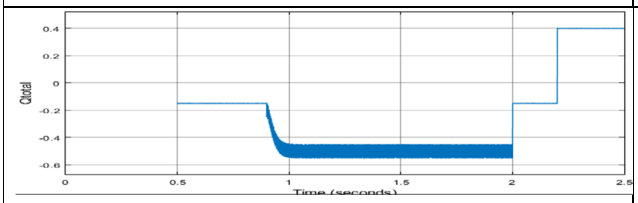

(e)Total output reactive power

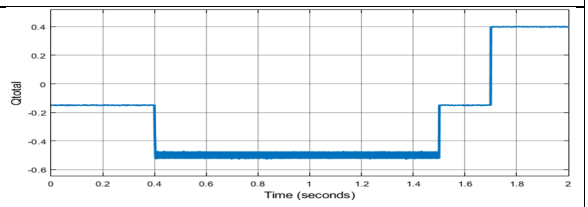

(e) Total output reactive power

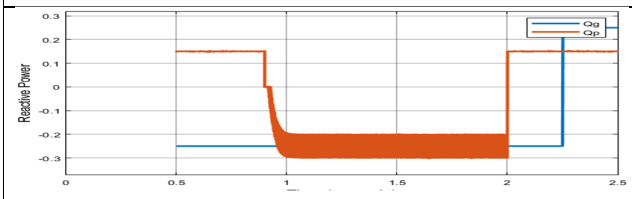

(f)PW and GSC reactive power

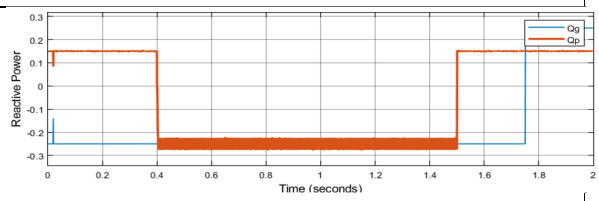

(f) PW and GSC reactive power

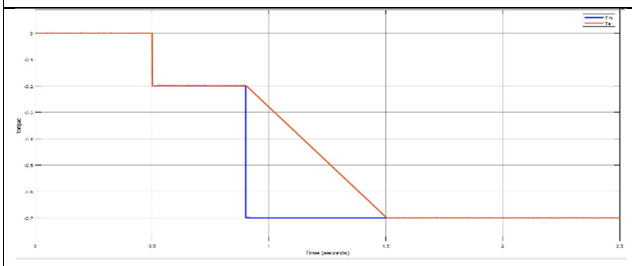

(g)Mechanical torque andElectromagnetic torque

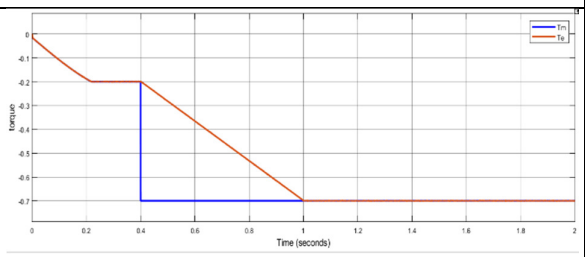

(g)Mechanical torque andElectromagnetic torque

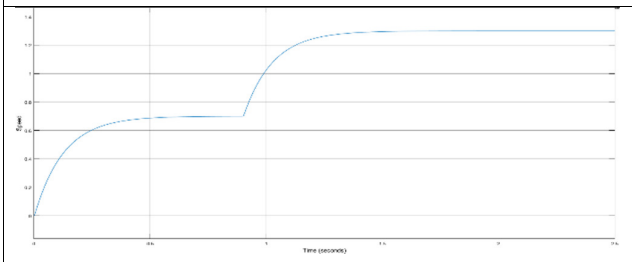

(h)Rotor rotating speed

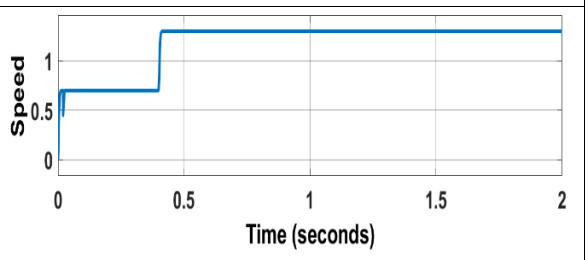

(h) Rotor rotating speed

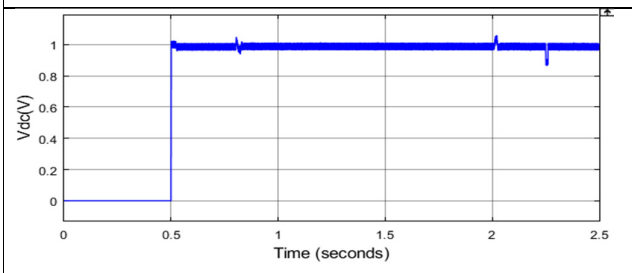

(i) Rotor rotating speed

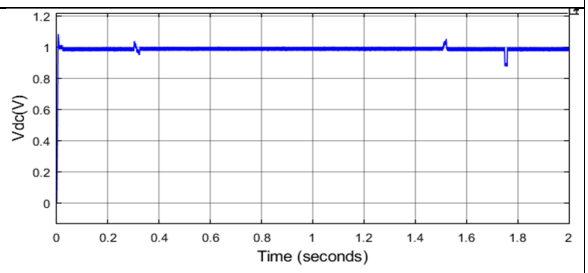

(i) Rotor rotating speed

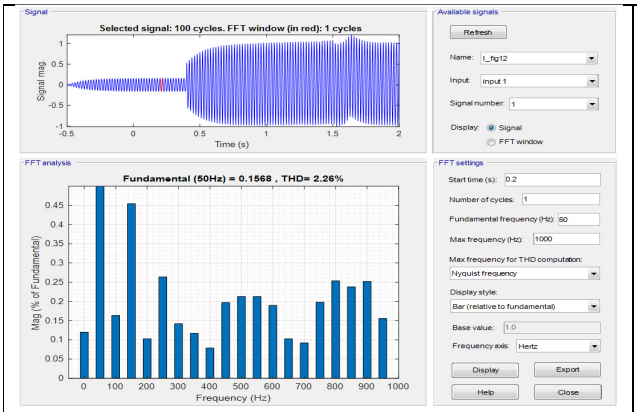

(j)THD value

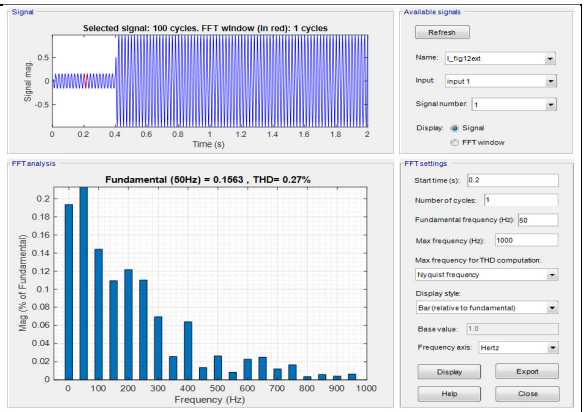

(j)THD value

FIGURE:15. Waveforms with variation of rotating speed under " D 10% grid voltage unbalance. (a) total output current (p.u.). (b) CW current (p.u.). (c) total output active power (p.u.). (d) PW and GSC active power (p.u.) (e) Total output reactive power (p.u.). (f) PW and GSC reactive power (p.u.). (g) Mechanical torque and electromagnetic torque (p.u.). (h) Rotor rotating speed (p.u.). (i) DC link voltage (p.u.).(j)THD value (p.u.).

XI.CONCLUSION:

This work presents a method for sensorless induction motor management that reduces torque ripple and extracts dc signals from dc current injections in the low-speed range. The analysis started with the flux ripple in the second harmonic current injection and arbitrary dc. The present reference, which eliminates torque fluctuation, is computed based on the study.. An averaging filter based on angle has been developed for the collection of DC current and voltage data. Basic flux rotor orientation is applied in the suggested solution to overcome the synchronous speed perturbation issue.. Simulation and simulation results verify the applicability of the proposed strategy. The suggested technique allows for an accurate estimation of the stator opposition, which is the most important parameter for the torque accuracy and stability of sensorless management of the Rechargeable Doubly-Fed Initiation Generators (BDFIG) at low speeds.

REFERENCE:

[1] Jang-Hwan Kim, Jong-Woo Choi and Seung-Ki Sul, "Novel rotor-flux observer using observer characteristic function in complex vector space for field-oriented induction motor drives," in IEEE Transactions on Industry Applications, vol. 38, no. 5, pp. 1334-1343, Sept.-Oct. 2002.

[2] L. Harnefors and M. Hinkkanen, "Stabilization Methods for Sensorless Induction Motor Drives—A Survey," in IEEE Journal of Emerging and Selected Topics in Power Electronics, vol. 2, no. 2, pp. 132-142, June 2014.

[3] V. Vasic, S. N. Vukosavic and E. Levi, "A stator resistance estimation scheme for speed sensorless rotor flux oriented induction motor drives," in IEEE Transactions on Energy Conversion, vol. 18, no. 4, pp. 476-483, Dec. 2003.

[4] M. S. Zaky, "Stability Analysis of Speed and Stator Resistance Estimators for Sensorless Induction Motor Drives," in IEEE Transactions on Industrial Electronics, vol. 59, no. 2, pp. 858-870, Feb. 2012.

[5] M. Hinkkanen, L. Harnefors and J. Luomi, "Reduced-Order Flux Observers With Stator-Resistance Adaptation for Speed-Sensorless Induction Motor Drives," in IEEE Transactions on Power Electronics, vol. 25, no. 5, pp. 1173-1183, May 2010.

[6] S. D. Wilson, G. W. Jewell and P. G. Stewart, "Resistance estimation for temperature determination in PMSMs through signal injection," IEEE International Conference on Electric Machines and Drives, 2005., San Antonio, TX, 2005, pp. 735-740.

[7] L. He, J. Restrepo, S. Cheng, R. G. Harley and T. G. Habetler, "An improved DC-signal-injection method with active torque-ripple mitigation for thermal monitoring of field-oriented-controlled induction motors," 2015 IEEE Energy Conversion Congress and Exposition (ECCE), Montreal, QC, 2015, pp. 4447-4454.

[8] F. Baneira, J. Doval-Gandoy, A. G. Yepes and O. López, "DC-Current Injection With Minimum Torque Ripple in Interior Permanent-Magnet Synchronous Motors," in IEEE Transactions on Power Electronics, vol. 35, no. 2, pp. 1176-1181, Feb. 2020.

[9] F. Baneira, A. G. Yepes, Ó. López and J. Doval-Gandoy, "Estimation Method of Stator Winding Temperature for Dual Three-Phase Machines Based on DC-Signal Injection," in IEEE Transactions on Power Electronics, vol. 31, no. 7, pp. 5141-5148, July 2016.

[10] P. R. Matić, M. A. Gecić, D. M. Lekić and D. P. Marčetić, "Thermal Protection of Vector-Controlled IM Drive Based on DC Current Injection," in IEEE Transactions on Industrial Electronics, vol. 62, no. 4, pp. 2082-2089, April 2015.

[11] S. Cheng, Y. Du, J. A. Restrepo, P. Zhang and T. G. Habetler, "A Nonintrusive Thermal Monitoring Method for Induction Motors Fed by Closed-Loop Inverter Drives," in IEEE Transactions on Power Electronics, vol. 27, no. 9, pp. 4122-4131, Sept. 2012.

[12] M. O. Sonnaillon, G. Bisheimer, C. D. Angelo and G. O. García, "Online Sensorless Induction Motor Temperature Monitoring," in IEEE Transactions on Energy Conversion, vol. 25, no. 2, pp. 273-280, June 2010.

[13] F. Baneira, L. Asiminoaei, J. Doval-Gandoy, H. A. M. Delpino, A. G. Yepes and J. Godbersen, "Estimation Method of Stator Winding Resistance for Induction Motor Drives Based on DC-Signal Injection Suitable for Low Inertia," in IEEE Transactions on Power Electronics, vol. 34, no. 6, pp. 5646-5654, June 2019.

[14] J. Faiz and M. B. B. Sharifian, "Different techniques for real time estimation of an induction motor rotor resistance in sensorless direct torque control for electric vehicle," in IEEE Transactions on Energy Conversion, vol. 16, no. 1, pp. 104-109, March 2001.

[15] P. Vaclavek and P. Blaha, "Lyapunov-function-based flux and speed observer for AC induction motor sensorless control and parameters estimation," in IEEE Transactions on Industrial Electronics, vol. 53, no. 1, pp. 138-145, Feb. 2006.